Nanoscale Advances

ROYAL SOCIETY OF CHEMISTRY

PAPER

View Article Online
View Journal | View Issue

Cite this: *Nanoscale Adv.*, 2025, **7**, 8093

Surface-modified iron oxide nanoprobes in biomedical scaffolds

M. A. González-Gómez, †*[a] Á. Arnosa-Prieto,†[a] P. García-Acevedo,[a] P. Diaz-Rodriguez,[b] L. de Castro-Alves,[a] Y. Piñeiro[a] and J. Rivas *[a]

Received 19th June 2025
Accepted 10th November 2025

DOI: 10.1039/d5na00605h

rsc.li/nanoscale-advances

Magnetic (PU) scaffolds incorporating superparamagnetic iron oxide nanoparticles (SPIONs) offer a promising platform for localized cancer therapy. By enhancing the functional performance of these scaffolds through surface modification of iron oxide nanoprobes, their biomedical utility—particularly in targeted therapeutic applications—can be significantly improved. In this study, we report the synthesis and characterization of magnetite nanoparticles (Fe_3O_4 NPs) functionalized with biocompatible coatings—citrate, polyethylene glycol (PEG), oleic acid (OA), and aluminum hydroxide ($Al(OH)_3$)—and their integration into porous PU scaffolds *via* a salt-leaching/phase-inversion method. Among all tested formulations, SPIONs@Al(OH) demonstrated superior colloidal stability, magnetic responsiveness, and cytocompatibility. When embedded in PU scaffolds, these magnetic nanocomposites exhibited optimal mesoporosity, homogeneous nanoparticle distribution, and efficient magnetic hyperthermia performance under clinically relevant alternating magnetic fields. This work highlights the synergistic potential of material design and surface engineering in developing next-generation implantable platforms for targeted oncological treatment.

1. Introduction

In recent years, nanotechnology has significantly influenced biomedical research, enabling novel diagnostic and therapeutic strategies based on nanostructured materials. Among these, magnetic nanoparticles (MNPs), particularly those composed of Fe_3O_4, stand out for their superparamagnetic behaviour, biocompatibility, and ease of functionalization, making them ideal for applications such as magnetic resonance imaging (MRI), targeted drug delivery, and magnetic hyperthermia therapy.[1–3]

Magnetic hyperthermia, based on the conversion of alternating magnetic field energy into localized heat, has emerged as a minimally invasive treatment option for solid tumors.[4] However, the clinical efficacy of this approach relies on the development of stable and biocompatible nanocarriers with sufficient magnetic responsiveness and colloidal stability under physiological conditions.[5,6] Surface modification plays a critical role in enhancing nanoparticle performance, preventing aggregation, and improving cellular interactions.

This study highlights the versatility of surface-functionalized iron oxide nanoparticles integrated into polyurethane scaffolds, suitable for magnetic hyperthermia treatments in medical settings.[7–9]

In this context, $Al(OH)_3$ coatings have demonstrated excellent ability to stabilize SPIONs, preventing oxidation and providing a hydrophilic and biocompatibility surface.[10,11] Moreover, their positive surface charge facilitates interaction with negatively charged cellular membranes, enhancing cellular uptake and therapeutic efficacy.[12–14]

Simultaneously, PU-based scaffolds are widely employed in biomedical engineering due to their mechanical robustness, tuneable porosity, and biocompatibility.[9] When doped with MNPs, these scaffolds can serve as multifunctional platforms for combined mechanical support and localized magnetic heating.[7,15] Previous studies incorporating unmodified MNPs into polymeric scaffolds such as PCL, PLA, or chitosan, often resulted in limited NPs dispersion and suboptimal biological performance.[16–19] These limitations highlight the need for systematic evaluation of surface-modified SPIONs within biocompatible matrices, such as PU, to enhance both magnetic and biological functionalities.

In this study, we synthesized a series of SPIONs, either bare or coated with citrate, PEG, OA, or $Al(OH)_3$, and incorporated them into PU scaffolds using a solvent casting and salt-leaching approach.[15] Recent reports have typically relied on a single surface modification, for example the use of PDA-coated Fe_3O_4 to enhance NPs dispersion and mechanical properties.[20]

[a]*NANOMAG Laboratory, Applied Physics Department, Materials Institute (iMATUS) and Health Research Institute (IDIS), Universidade de Santiago de Compostela, Santiago de Compostela, 15782, Spain. E-mail: manuelantonio.gonzalez@usc.es; jose.rivas@usc.es*

[b]*I+D Pharma Group (GI-1645), Department of Pharmacology, Pharmacy, and Pharmaceutical Technology, Institute of Materials (iMATUS), Universidade de Santiago de Compostela, Santiago de Compostela, 15782, Spain*

† These authors are considered as co-first authors.

However, such approaches provide only a limited perspective on how surface chemistry modulates scaffold performance. In this work, we systematically examine multiple surface modifications (citrate, PEG, OA, and $Al(OH)_3$) thereby enabling direct correlations between nanoparticle coating, scaffold stability, magnetic hyperthermia efficiency, and cytocompatibility. This comparative framework offers deeper insight into NPs-scaffold interactions and identifies SPIONs@$Al(OH)_3$ as the most promising formulation for biomedical applications.

2. Experimental section

2.1 Materials

Iron(II) sulfate heptahydrate (99%), iron(III) chloride hexahydrate (99%), ammonium hydroxide solution (28%), oleic acid (90%), cyclohexane (99%), aluminum nitrate nonahydrate (98%), *N*,*N*-dimethylformamide (DMF, 99.8%), sodium chloride (99.5%), urea (99%), sodium citrate tribasic dihydrate (98%), glycerol ethoxylate (PEG, with molecular weight average M_W 1000), dibutyltin dilaurate (DBTDL, 95%), isophorone diisocyanate (IPDI, 98%) and L-cystine dimethyl ester dihydrochloride (95%), sodium hydroxide (97%) and ethanol (absolute grade) were purchased from Merck. Aluminum sulfate hexadecahydrate (95%) and ethyl acetate (99%) were obtained from Fluka. Hydrochloric acid (37%) was obtained from Acros Organics. Dulbecco's Modified Eagle Medium (DMEM), fetal bovine serum, and Dulbecco's modified phosphate buffered saline (DPBS) were obtained from Gibco. Penicillin/streptomycin was purchased from Thermo Fisher. Milli-Q (Millipore®) deionized water and cell culture grade water purchased from Corning were used in all the experiments. Chemicals were used as received, without additional purification.

2.2 Synthesis

Magnetic PU scaffolds were prepared *via* a sequential route: (i) co-precipitation of single-core SPIONs with optional citrate/PEG/OA surface modification; (ii) forced chemical hydrolysis to obtain SPIONs@$Al(OH)_3$; and (iii) salt-leaching/phase-inversion to embed SPIONs in PU (Scheme 1). Sample codes MS1–MS5 and SPIONs loadings/solvents are summarized in Table 1.

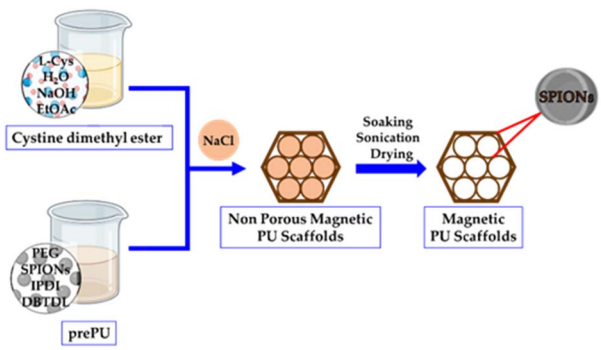

Scheme 1 Schematic illustration of the synthesized magnetic PU scaffolds obtained through their corresponding method.

Table 1 Solvents used for the suspension of MNPs according to their addition step in the synthetic procedure of the magnetic scaffolds (MS)

Magnetic scaffold	MNPs	Solvent	Mass of MNPs (g)
MS1	Uncoated SPIONs	PEG	0.1
MS2	SPIONs@citrate	PEG	0.1
MS3	SPIONs@PEG	PEG	1.0
MS4	SPIONs@OA	DMF	1.0
MS5	SPIONs@$Al(OH)_3$	DMF	0.7

2.2.1 Synthesis of single-core SPIONs (uncoated; citrate, PEG, or OA-coated). The synthesis was performed using a co-precipitation method based on the procedure described by Massart.[21,22] $FeCl_3 \cdot 6H_2O$ (45 mmol) and $FeSO_4 \cdot 7H_2O$ (30 mmol) were dissolved in HCl (100 mL, 10 mM) under mechanical stirring at 220 rpm for 15 minutes at room temperature. The temperature was then increased to 60 °C, followed by the addition of NH_4OH (30 mL). The reaction was allowed to proceed for 30 minutes, resulting in the formation of Fe_3O_4 NPs with an average size of 10 nm. At this stage, a stabilizing agent can be introduced into the NPs solution to obtain coated NPs. In this work, we developed both bare magnetic NPs and a series of NPs coated with sodium citrate, PEG, or OA. These coating agents were added at a concentration of 1.11 mmol and incubated for 1 hour at 60 °C. Subsequently, the bare or coated magnetic NPs were acidified to pH 5 using a 9% HCl solution. The uncoated and functionalized magnetite NPs were separated from the reaction medium using a magnetic field and washed thoroughly with Milli-Q water (6 times) to remove impurities. Finally, the obtained NPs were suspended in cell culture-grade water for further use.

2.2.2 Synthesis of SPIONs@$Al(OH)_3$ (multicore@shell). The $Al(OH)_3$ coating on bare Fe_3O_4 NPs was carried out through a modified forced chemical hydrolysis method, which included the addition of bare Fe_3O_4 NPs to the reaction mixture.[23] Briefly, 200 mg of Fe_3O_4 NPs were dispersed in 250 mL of Milli-Q water using sonication for 15 minutes to achieve a homogeneous suspension. Subsequently, $Al(NO_3)_3 \cdot 9H_2O$ (11.6 mmol), $Al_2(SO_4)_3 \cdot 16H_2O$ (1.92 mmol), and urea (0.5 mol) were added to the solution. The reaction mixture was heated in an oil bath at 98 °C under mechanical stirring for 1.5 hours. After the reaction, the resulting multi_core@shell magnetic NPs was magnetically separated, washed six times with Milli-Q water to remove impurities, and finally re-dispersed in cell culture-grade water for further use.

2.2.3 Synthesis of magnetic PU scaffolds (MS1–MS5). PU scaffolds were prepared using the salt leaching-phase inversion technique with a modified approach for the incorporation of MNPs of the procedure described by Zhou *et al.*[24] First, L-cystine dimethyl ester dihydrochloride (29.3 mmol) was dissolved in water (10 mL) and the pH was adjusted to 9 by addition of NaOH (0.1 M). Then the solution was extracted with ethyl acetate. After evaporating the solvent by vacuum distillation until a volume of 2 mL, the cystine dimethyl ester was used directly with no further purification.

PEG (4.8 mmol) and IPDI (14.2 mmol) were mixed at 70 °C for 1 hour under N_2 atmosphere and vigorous mechanical stirring. DBTDL (630 nmol) was added, and the mixture was stirred for 1 hour under the same conditions achieving the polyurethane precursor (prePU). Then, prePU was dissolved in DMF (10 mL). NaCl particles (100–150 μm, 5 g) and cystine dimethyl ester (390 μL dissolved in 5 mL DMF) were added to the prePU solution under vigorous mechanical stirring. After one minute, polymerization was achieved. In a critical step to remove DMF and NaCl, the obtained PU scaffold (PS) was soaked in water for 3 days and, afterwards, washed with an ethanol : water 1 : 1 mixture using sonication for 15 min in the sonication bath and a probe sonicator for 10 s. Then, the PU scaffold was left for 2 days with orbital shaking. The procedure was repeated two more times using an ethanol : water 5 : 2 mixture. Finally, the PU scaffold (PS) was air dried.

MNPs were incorporated either *via* PEG (added in the first step) or *via* DMF (added to the pre-PU solution). Table 1 summarises SPION type, solvent, and mass (MS1–MS5). For each scaffold, the MNP loading corresponded to the highest amount compatible with stable, homogeneous foaming (no phase separation or collapse).

2.3 Physicochemical characterization

2.3.1 SPIONs. Morphology, crystallinity, surface chemistry, dynamic light scattering, surface charge, compositional and magnetic properties of the developed SPIONs (SPIONs@citrate, SPIONs@PEG, SPIONs@OA, and SPIONs@Al(OH)$_3$) were characterized prior to scaffold incorporation.

High-resolution Transmission Electron Microscopy (HRTEM) selected area electron diffraction (SAED) were performed using a Carl Zeiss Libra 200 FE (Carl Zeiss Iberia, Madrid, Spain) microscope (200 kV) on dried nanoparticle suspensions.

X-ray diffraction (XRD) patterns were recorded with a Philips/Panalytical diffractometer using Cu Kα radiation ($\lambda = 1.5406$ Å), 2θ range 10–80°, 0.02° step, and 5 s acquisition time per step. The crystallite size was determined from the broadening of the XRD peaks using Scherrer's equation:[25]

$$d = \frac{k\lambda}{\beta \cos \theta_{hkl}} \quad (1)$$

where d represents the average crystallite size (nm), k is the dimensionless Scherrer constant (0.9), λ corresponds to the X-ray wavelength used, β denotes the full width at half maximum (FWHM, in radians) of the diffraction peak, and θ is the Bragg angle (degrees).

Fourier transform infrared (FT-IR) spectra were collected using a Thermo Nicolet Nexus spectrometer (Thermo Fisher Scientific, Madrid, Spain) equipped with an attenuated total reflectance (ATR) accessory, covering the spectral range of 400–4000 cm^{-1}.

Dynamic Light Scattering (DLS) and ζ-potential were measured on a Zetasizer Nano ZS (Malvern) at 25 °C using disposable cuvettes and 173° backscatter detection; values reported are averages of triplicate runs.

Thermogravimetric analysis (TGA) was performed on a PerkinElmer 8000 under a nitrogen flow of 20 mL min^{-1}, heating from 50 °C to 850 °C at a rate of 10 °C min^{-1}, to estimate the organic coating content.

The Fe concentration was determined by inductively coupled plasma optical emission spectrometry (ICP-OES) using a PerkinElmer Optima 3300 DV spectrometer (PerkinElmer, Waltham, MA, USA).

Vibrating sample magnetometry (VSM) (DMS system, ±10 kOe, RT) was used to determine saturation magnetization (M_s) normalized to the magnetic mass of the MNPs.

2.3.2 Magnetic polyurethane (PU) scaffolds. After MNPs incorporation, the structural, morphological, and magnetic features of the PU-based magnetic scaffolds (MS1–MS5) were analyzed.

Scanning electron microscopy (SEM) using a ZEISS FE-SEM ULTRA Plus (30 kV) (Zeiss, Oberkochen, Germany) was employed to visualize the porous architecture of PU-based scaffolds, with and without embedded SPIONs.

Pore size distribution and interconnectivity of the magnetic 3D scaffolds were defined by mercury porosimetry using an AutoPore IV 9500 V1.09 system (Micromeritics, Norcross, GA, USA).

FT-IR spectra of the PU-based scaffolds were acquired on a Thermo Nicolet Nexus spectrometer using the same experimental conditions employed for the MNPs.

Magnetic characterization of the scaffolds was performed by VSM under the same field range as for MNPs; magnetization values were normalized to total scaffold mass.

ICP-OES (bulk content). Scaffolds were acid-digested (65% HNO_3, 80 °C) and analyzed by ICP-OES (Optima 3300 DV, PerkinElmer, Waltham, MA, USA) to determine Fe content; Fe_3O_4 mass was calculated from Fe stoichiometry. The Fe_3O_4 contents for MS1–MS5 are summarized in Table 4.

ICP-OES (leachability, MS5). Scaffolds were stored under the conditions described later in Section 3.3 (Magnetic hyperthermia performance); supernatants were analyzed after 3 months. Dissolved Fe was below the instrument detection limit (DL). DLS are provided in the SI.

2.4 Magnetic hyperthermia measurements

Magnetic hyperthermia was evaluated using a MagneTherm system (Nanotherics, Warrington, UK) equipped with a water-cooled hollow induction coil. PU-based magnetic scaffolds were centred within the coil to ensure optimal exposure to the RF magnetic field, and temperature was monitored in real time with a fibre-optic probe (non-invasive). All experiments were performed under an alternating magnetic field of $H = 25$ mT (≈ 20 kA m^{-1}) at $f = 253$ kHz. For each sample, the temperature evolution was recorded for 5 min with the field on, followed by 2 min with the field off to capture the cooling profile. The SAR was calculated from the initial heating slope ($\Delta T/\Delta t$), using the specific heats of magnetite and PU and the Fe_3O_4 mass fraction per scaffold, as detailed in the Results and discussion section.

2.5 Toxicity evaluation of magnetic PU-based scaffolds

The toxicity of magnetic PU scaffolds was assessed to evaluate their suitability as implantable devices. Cytocompatibility of

SPION-loaded scaffolds (MS5) and blank scaffolds (PS) was tested on murine NIH/3T3 fibroblasts (ATCC CRL-1658) under direct and indirect contact conditions. Experiments were performed following ISO 10993-5:2009 guidelines where direct experiments are performed by the culture of cells in the presence of scaffolds whereas indirect experiments were performed by placing the samples in inserts hanging in wells of 24-well plates and cells were cultured on the bottom of the wells.

Cells were cultured in complete DMEM (DMEM, Gibco) supplemented with 10% fetal bovine serum (Gibco) and 1% penicillin/streptomycin, seeded in 24-well plates at 1.0×10^5 cells per well, and allowed to adhere for 24 h. Prior to cell exposure, scaffolds were washed with DPBS and pre-equilibrated in complete medium at 37 °C for 2 h. For direct contact, samples were placed onto the cell monolayers; for indirect contact, samples were transferred to polycarbonate inserts (8 μm pore size) positioned in the corresponding wells containing cell monolayers. After 24 h, cell viability was quantified using the Cell Counting Kit-8 following the manufacturer's instructions, and absorbance was read at 450 nm; values were normalized to untreated controls (set to 100%). Four replicates were analysed for each condition.

3. Results and discussion

3.1 Magnetic NPs

TEM analysis confirms that uncoated SPIONs are quasi-spherical with noticeable aggregation and an average core size of approximately 10 nm (Fig. 1a), consistent with their high surface energy and the absence of a stabilising layer. Functionalisation with citrate (Fig. 1b) and oleic acid (OA, Fig. 1d) yields more homogeneous particle distributions, whereas clustering remains evident for SPIONs@PEG (Fig. 1c). These coatings enhance colloidal stability through a combination of electrostatic repulsion (in the case of citrate) and steric hindrance (for PEG and OA), reducing particle agglomeration in suspension. This trend is reflected in the DLS and ζ-potential values reported in Table 2, with the hydrodynamic size and surface charge distributions provided in Fig. S2–S6 (SI).[1,26,27] These observations emphasize the key role of surface chemistry in tuning the aggregation behavior and stability of MNPs for biomedical applications.

Table 2 Hydrodynamic size (D_H), polydispersity index (PDI) and ζ-potential the synthesized SPIONs

Sample	D_H (nm)	PDI	ζ-potential (mV)
Uncoated SPIONs	109.90	0.36	−24.80
SPIONs@citrate	23.41	0.23	−42.50
SPIONs@PEG	67.77	0.20	−57.20
SPIONs@OA	33.95	0.25	−32.70
SPIONs@$Al(OH)_3$	256.90	0.42	12.80

SPIONs functionalized with $Al(OH)_3$ (Fig. 2a) exhibited a markedly distinct morphology compared to the rest of the synthesized SPIONs. The TEM micrographs reveal the formation of large multicore MNPs embedded with a inorganic shell with an overall average diameter of approximately 200 nm. This formation is promoted by ionic interactions and hydrogen bonding mediated by the hydroxyl-rich aluminum hydroxide shell, which acts as a bridging framework between adjacent MNPs.[10]

High-resolution HRTEM imaging (Fig. 2c) further confirms the crystalline nature of the Fe_3O_4 cores. The observed lattice fringes correspond to an interplanar spacing of approximately 0.20 nm, which matches the (400) crystallographic planes of magnetite, consistent with an inverse spinel-type crystal structure.[28]

The selected area electron diffraction (SAED) pattern of single-core SPIONs synthesized *via* the co-precipitation method

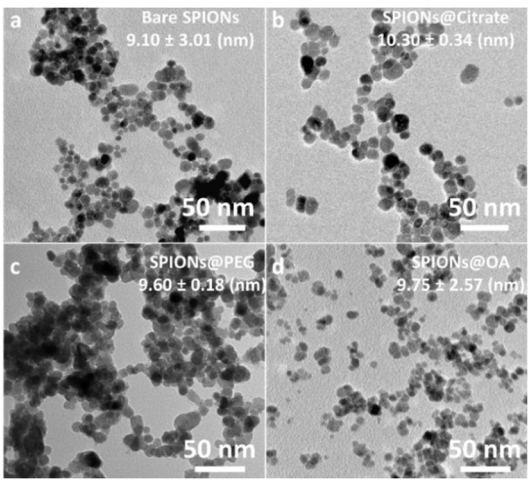

Fig. 1 TEM micrographs of single-core SPIONs: (a) uncoated, and surface-functionalized with (b) citrate, (c) PEG, and (d) OA. Size distribution histograms are provided in Fig. S1 (SI).

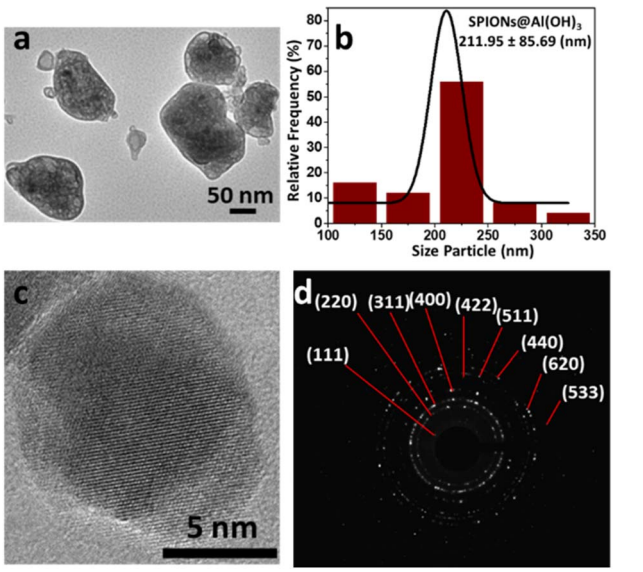

Fig. 2 Morphological and structural characterization of SPIONs@$Al(OH)_3$. (a) TEM image, (b) size distribution histogram, (c) HRTEM image and (d) SAED pattern of single-core SPIONs.

(Fig. 2d) exhibits concentric diffraction rings, which can be indexed to the (111), (220), (311), (400), (422), (511), (440), (620), and (533) planes of the cubic spinel structure of Fe_3O_4.

The powder XRD patterns of bare SPIONs, SPIONs@citrate, SPIONs@PEG, SPIONs@OA, and SPIONs@Al(OH)$_3$ NPs are shown in Fig. 3a, along with the reference pattern for magnetite (Inorganic Crystal Structure Database, ICSD, card No. 98-015-8742).[29] The diffraction peaks observed at 18.4°, 30.2°, 35.6°, 37.2°, 43.3°, 53.7°, 57.2°, 62.8°, 71.3°, and 74.4° can be indexed to the (111), (220), (311), (400), (422), (511), (440), (620), and (553) planes of the cubic spinel structure of Fe_3O_4, respectively.[30]

The position and relative intensity of the peaks match well with the standard reference and previously reported data, confirming the formation of phase-pure magnetite NPs.[31] The average crystallite sizes, calculated from the (311) reflection using the Scherrer equation, were estimated to be 6.68 nm for uncoated SPIONs, 6.49 nm for SPIONs@citrate, 6.99 nm for SPIONs@PEG, 6.66 nm for SPIONs@OA, and 6.67 nm for SPIONs@Al(OH)$_3$ NPs.

The FT-IR spectra of the synthesized SPIONs are displayed in Fig. 3b. All samples exhibit characteristic absorption bands at 538 cm^{-1} and 629 cm^{-1}, corresponding to the stretching vibrations of Fe–O bonds, confirming the presence of Fe_3O_4.[32] The spectrum of uncoated SPIONs further shows absorption bands at approximately 1003 cm^{-1}, 1630 cm^{-1}, and 3410 cm^{-1}, which can be assigned to deformation, bending, and stretching modes of surface hydroxyl groups, respectively.[33,34] In the case of SPIONs@citrate NPs, the presence of a band at 1066 cm^{-1} corresponds to C–H vibrations, while two distinct bands in the 1330–1400 cm^{-1} and 1560–1570 cm^{-1} range, are attributed to the symmetric and asymmetric stretching vibrations of the carboxylate (COO^-) groups of citrate, respectively as reported in the literature.[35,36] A broad band centred around 3370 cm^{-1} is associated with structural –OH groups and residual adsorbed water.[36] For SPIONs@PEG NPs, a band near 1488 cm^{-1} is assigned to C–C stretching vibrations, while a signal at 1639 cm^{-1} corresponds to CH_2/CH_3 bending modes. A broad band at 3425 cm^{-1} is indicative of –OH stretching, in agreement with PEG surface coverage.[37,38] The FT-IR spectrum of SPIONs@OA NPs displays an absorption at 1044 cm^{-1} due to C–O stretching, and bands at 1511 cm^{-1} and 1588 cm^{-1} corresponding to the symmetric and asymmetric stretching of the carboxylate groups, respectively.[39] Additionally, peaks at 2853 cm^{-1} and 2913 cm^{-1} are assigned to symmetric and asymmetric CH_2 stretching vibrations, consistent with the alkyl chains of oleic acid.[40] Finally, the SPIONs@Al(OH)$_3$ NPs exhibit a peak at 1101 cm^{-1}, attributed to Al–O bond stretching, and a broad absorption band around 3400 cm^{-1} associated with surface –OH groups, likely from adsorbed water and Al(OH)$_3$ shell hydroxyls.[41]

The magnetization values were normalized to the magnetic mass content of each sample. Fig. 4 displays the room-temperature hysteresis loops of uncoated SPIONs, SPIONs@citrate, SPIONs@PEG, SPIONs@OA, and SPIONs@Al(OH)$_3$. The corresponding saturation magnetization (M_s), remanent magnetization (M_r), and coercivity (H_C) values are summarized in Table 3.

As expected, all samples exhibited lower M_s values compared to bulk magnetite (M_s_bulk = 92–100 emu g^{-1}), which can be

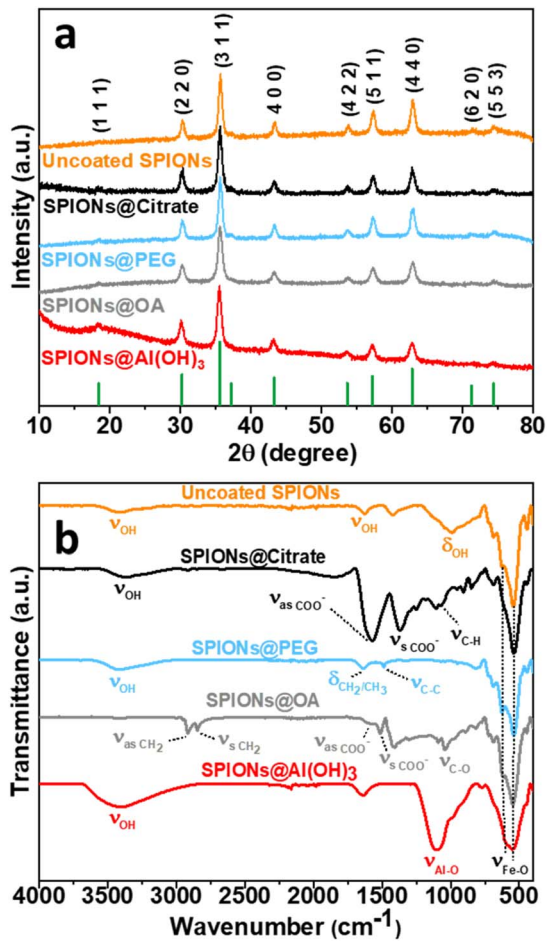

Fig. 3 (a) XRD patterns and (b) FT-IR spectra of uncoated SPIONs (orange) and SPIONs NPs functionalized with citrate (black), PEG (blue), OA (grey), and Al(OH)$_3$ (red).

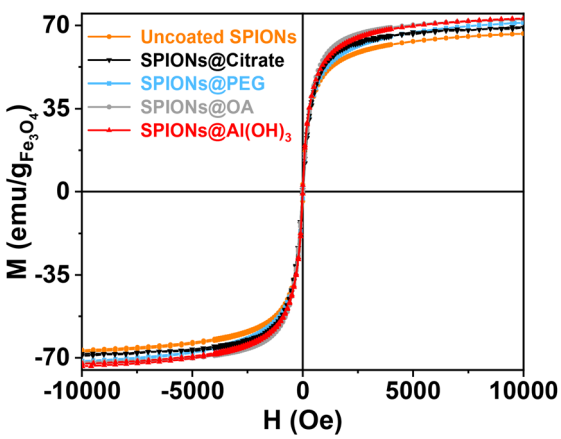

Fig. 4 Room-temperature hysteresis loops of SPIONs with different surface coatings: uncoated (orange), citrate (black), PEG (blue), OA (grey), and Al(OH)$_3$ (red), all exhibiting superparamagnetic behavior.

Table 3 Magnetic parameters of the synthesized SPIONs with different surface coatings: saturation magnetization (M_s), remanent magnetization (M_r), and coercivity (H_c), as determined from room-temperature hysteresis loops

Sample	M_s (emu g^{-1})	M_r (emu g^{-1})	H_c (Oe)
Uncoated SPIONs	66.84	3.40	20.42
SPIONs@citrate	68.71	0.83	6.16
SPIONs@PEG	71.40	2.29	14.83
SPIONs@OA	72.36	0.42	2.92
SPIONs@Al(OH)$_3$	73.21	1.59	8.02

attributed to their nanoscale dimensions and the presence of a magnetically inactive surface layer (dead magnetic layer) that reduces the overall magnetization.[42–44] The measured M_s values ranged from 66.8 to 73.2 emu g^{-1}, in good agreement with values reported for magnetite nanoparticles synthesized *via* similar routes.[22,45]

Although the overall M_s values are comparable across the different samples, slight variations were observed, with the lowest value corresponding to uncoated SPIONs (66.8 emu g^{-1}) and the highest to SPIONs@Al(OH)$_3$ NPs (73.2 emu g^{-1}). These differences are likely influenced by the nature of the surface coatings, which can affect nucleation, growth kinetics, and ultimately the magnetic domain structure of the MNPs. In particular, the higher magnetization observed for SPIONs@Al(OH)$_3$ may also be attributed to their multicore architecture, where several magnetite nanocrystals are assembled within a single particle. This structural configuration can enhance interparticle magnetic coupling and reduce surface spin disorder, leading to improved overall magnetic performance.[46,47] All samples displayed negligible remanence and coercivity, confirming their superparamagnetic behavior at room temperature.

3.2 Magnetic polyurethane scaffolds

The control scaffold (Fig. 5a) appears white, corresponding to the unmodified PU matrix. In contrast, scaffolds loaded with MNPs (Fig. 5b–f) exhibit varying brownish tones, reflecting the incorporation and distribution of the different surface-functionalized Fe_3O_4 NPs within the polymeric structure.

The differences in colour intensity may be attributed to variations in surface chemistry, nanoparticle dispersion, and interaction with the PU matrix, suggesting successful incorporation of the MNPs in all formulations.

Fig. 6 presents SEM micrographs of the fabricated polyurethane-based scaffolds, revealing a mesoporous architecture characterized by interconnected pores of heterogeneous sizes. Overall, two distinct pore size populations can be identified, as summarized in Table 4.

Most scaffolds including those containing uncoated SPIONs, SPIONs@citrate, SPIONs@PEG, and SPIONs@Al(OH)$_3$ exhibit a first group of smaller pores with average diameters ranging from 17 to 47 μm. Additionally, all scaffolds present a second group of larger pores, with mean sizes between 99 and 191 μm, depending on the type of incorporated MNPs.

Notably, the scaffold containing SPIONs@OA deviates from this trend, lacking the smaller pore population. These structural differences suggest that the surface chemistry of the nanoparticles influences the pore formation process during scaffold fabrication, potentially affecting their mechanical properties and suitability for specific biomedical applications such as cell infiltration or nutrient diffusion.

Fig. 7 presents the FT-IR spectra of the synthesized magnetic PU-based scaffolds. The broad absorption band at 3334 cm^{-1} corresponds to the N–H stretching vibration of the urethane

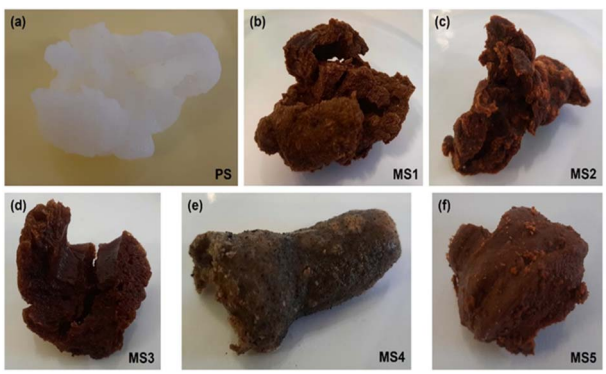

Fig. 5 Representative images of the polyurethane (PU) scaffold alone (a) and PU scaffolds incorporating various Fe_3O_4-based nanoparticles: (b) uncoated SPIONs, (c) SPIONs@citrate, (d) SPIONs@PEG, (e) SPIONs@OA, and (f) SPIONs@Al(OH)$_3$.

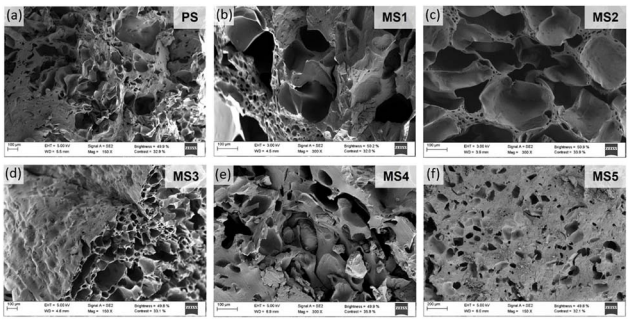

Fig. 6 SEM micrographs of the polyurethane scaffold (PS, (a)) and polyurethane scaffolds incorporating MNPs: uncoated (MS1, (b)), citrate (MS2, (c)), PEG (MS3, (d)), OA (MS4, (e)), and Al(OH)$_3$ (MS5, (f)).

Table 4 Average pore sizes of the two distinct pore populations observed in the PU-based scaffolds, as determined from SEM micrographs. Measurements were performed using ImageJ software by calculating the mean diameters from multiple representative images

Scaffold	Small pores (μm)	Big pores (μm)
PS	17 ± 7	131 ± 44
MS1	19 ± 7	183 ± 52
MS2	15 ± 4	191 ± 61
MS3	46 ± 11	180 ± 63
MS4	—	99 ± 37
MS5	27 ± 10	106 ± 27

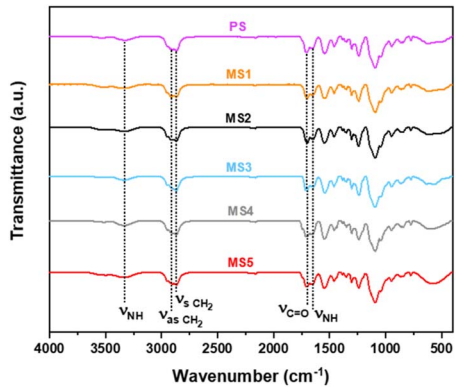

Fig. 7 FT-IR spectra of the obtained polyurethane scaffolds without and with magnetic material, identifying the most characteristic absorption bands. PS stands for polyurethane scaffold. MS1, MS2, MS3, MS4, MS5 represent magnetic scaffolds containing uncoated SPIONs, SPIONs@citrate, SPIONs@PEG, SPIONs@OA, and SPIONs@Al(OH)$_3$, respectively.

group. Characteristic bands of the asymmetric and symmetric stretching vibrations of CH_2 groups are observed at 2914 cm^{-1} and 2867 cm^{-1}, respectively.[15] The absorption peak at 1705 cm^{-1} is attributed to the C=O stretching of the urethane linkage, while the band at 1648 cm^{-1} is assigned to the N–H bending vibration of the amide group.[48] Notably, no signal is detected around 2270 cm^{-1}, indicating the absence of unreacted isocyanate (N=C=O) groups and confirming the complete formation of urethane bonds.[49] depending on the type of incorporated MNP.

The scaffolds labelled MS1 to MS5 contain the MNPs previously described and characterized in Fig. 3b, namely uncoated SPIONs (MS1), SPIONs@citrate (MS2), SPIONs@PEG (MS3), SPIONs@OA (MS4), and SPIONs@Al(OH)$_3$ (MS5). Although the major absorption bands correspond to the PU matrix, the successful incorporation of MNPs is evidenced by subtle variations in band intensity and shape, particularly in the 500–600 cm^{-1} region, associated with Fe–oxygen interactions.[10]

Fig. 8 shows the hysteresis loops of all the scaffolds containing MNPs, with the corresponding values of M_s, M_r, and H_c

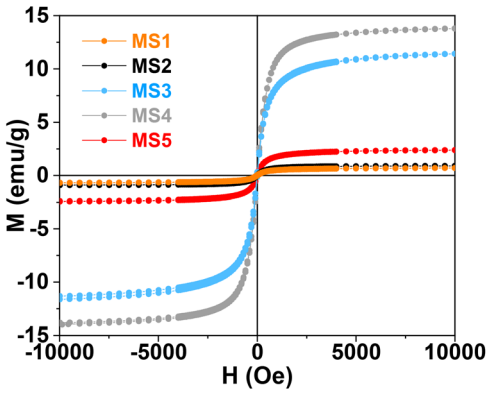

Fig. 8 Hysteresis loops of PU scaffolds containing MNPs at room temperature, showing superparamagnetic behavior. MS1–MS5 correspond to scaffolds with SPIONs: uncoated (MS1), citrate (MS2), PEG (MS3), OA (MS4), and Al(OH)$_3$ (MS5), respectively.

listed in Table 4. Note that M_s values are not normalized to MNP mass (unlike Fig. 3). Accordingly, the lower M_s for scaffolds with uncoated/citrate SPIONs reflects their lower loading (100 mg) relative to PEG/OA-coated samples (1 g) during synthesis. In addition to M_s, we report H_c, which spans around 5–30 Oe: MS1 (uncoated) shows the highest H_c, whereas MS4 (OA-coated) the lowest. This trend can be attributed to surface chemistry and interparticle coupling effects uncoated/citrate samples exhibit stronger dipolar interactions and surface-induced anisotropy, while PEG/OA shells reduce coupling and effective anisotropy, yielding lower H_c and behavior closer to superparamagnetism at 300 K.[50–52]

Interestingly, the M_s value for the magnetic scaffold containing SPIONs@Al(OH)$_3$ NPs is not as high as those for scaffolds doped with PEG or OA-coated MNPs, despite the addition of 700 mg of NPs. This discrepancy is likely due to the lower proportion of iron oxide in SPIONs@Al(OH)$_3$ NPs (only 15%), compared to the 80–90% of iron oxide present in the other NPs.

When comparing the M_s values of the MNPs used in the fabrication of these magnetic nanocomposites, we can estimate the total amount of magnetic material within the PU scaffolds. The M_s values for scaffolds containing uncoated SPIONs, SPIONs@citrate, SPIONs@PEG, SPIONs@OA, and SPIONs@Al(OH)$_3$ NPs were 1.02%, 1.32%, 16.11%, 19.25%, and 2.92%, respectively. This data demonstrates that the MS exhibit varying magnetic responses to external stimuli, with the strongest responses observed in MS doped with Fe_3O_4@OA NPs (M_{max} = 13.86 emu g^{-1}), in contrast to those doped with bare Fe_3O_4 NPs (M_{max} = 0.70 emu g^{-1}).

Regarding H_c, although the H_c values differ from those of the isolated MNPs, likely due to experimental conditions, the general trend is maintained. The scaffold doped with uncoated SPIONs exhibits the highest coercivity (H_c = 29.48 Oe), while the MS doped with SPIONs@OA NPs shows the lowest coercivity value (H_c = 5.40 Oe). These findings reflect how coating and composition modulate the scaffold magnetic response *via* surface passivation, interparticle spacing (dipolar coupling), and magnetic volume fraction. Consequently, uncoated/citrate samples show higher H_c, PEG/OA coatings yield lower H_c, and thick non-magnetic shells (Al(OH)$_3$) reduce the apparent M_s as reported in previous studies.[53–55]

3.3 Magnetic hyperthermia performance

The heating curves of the scaffolds doped with uncoated SPIONs, SPIONs@citrate, SPIONs@PEG, SPIONs@OA, and SPIONs@Al(OH)$_3$ are shown in Fig. 9. The data reveal substantial differences in thermal response depending on the surface functionalization of the MNPs. Notably, PU scaffolds incorporating SPIONs@Al(OH)$_3$ exhibited the most efficient thermal performance, achieving the highest temperature increase (ΔT) under the same field conditions. This superior heating efficiency can be attributed to the multicore architecture of the SPIONs@Al(OH)$_3$, which promotes stronger interparticle magnetic coupling and reduces surface spin disorder, thus enhancing magnetic loss mechanisms.

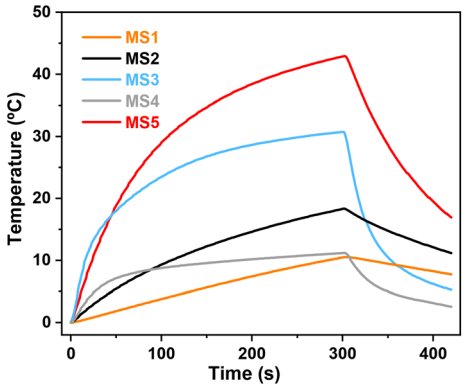

Fig. 9 Magnetic hyperthermia performance of polyurethane scaffolds doped with uncoated SPIONs (MS1), SPIONs@citrate (MS2), SPIONs@PEG (MS3), SPIONs@OA, and SPIONs@Al(OH)$_3$ (MS5). After 300 s the field was switched off, and the subsequent profile corresponds to the cooling curve of the samples. Field parameters were selected close to the biomedical safety threshold ($H \times f \approx 5.0 \times 10^9$ A m^{-1} s^{-1}).[56,57]

In contrast, scaffolds containing uncoated SPIONs or those coated with PEG and OA exhibited more modest temperature increases, consistent with a weaker magnetic response and reduced specific absorption rate (SAR).

The scaffold loaded with SPIONs@citrate displayed intermediate behavior, likely due to partial stabilization and magnetic decoupling effects introduced by the citrate layer. These findings demonstrate the critical influence of surface chemistry and particle architecture on the magnetic heating efficiency of nanoparticle-doped scaffolds, with direct implications for the design of hyperthermia-capable nanocomposite systems biomedical therapy.

From the heating curves it was possible to study the heating efficiency by determining the SAR, obtained experimentally by the follow equation:[30].

$$\mathrm{SAR} = \frac{m_{Fe_3O_4} C_{Fe_3O_4} + m_{PU} C_{PU}}{m_{Fe_3O_4}} \left(\frac{\Delta T}{\Delta t}\right)_0 \quad (2)$$

where $m_{Fe_3O_4}$ and m_{PU} are the mass of iron oxide and the mass of polyurethane present in the magnetic scaffolds, respectively, calculated from the total mass of each sample and considering iron oxide weight percentage; $C_{Fe_3O_4} = 0.746$ (J g^{-1} K^{-1}) and C_{PU} = 1.4 (J g^{-1} K^{-1}) are the specific heat of magnetite and polyurethane, respectively.

The SAR values obtained by eqn (2), compiled in Table 5, differ from the maximum temperature increments, ΔT, obtained. While sample MS5 reached the highest ΔT (ΔT = 42.86 °C) and thus revealed to have a higher SAR (SAR = 18.21 W g^{-1}), which can be attributed to its multicore nanoparticle architecture and enhanced magnetic coupling within the scaffold matrix.[2] the ΔT of MS2 does not correspond to the high SAR value obtained (SAR = 12.64 W g^{-1}). In this sense, sample MS3, with a significantly lower SAR revealed a ΔT almost twice as high as MS2. The main reason explaining these effects lies in the way the SAR is determined, where $\Delta T/\Delta t$ is selected at the beginning of the heating ramp. Therefore, differences in heat diffusion losses, which lead to a higher or lower increase in T, are not reflected in the SAR. On the other hand, the use of different amounts of magnetic material and the arrangement of the MNPs in the polyurethane matrix may lead to a different heat diffusion in the material.

Due to their superior efficiency, MS3 and MS5 both achieved ΔT > 30 °C, with PU scaffolds containing SPIONs@Al(OH)$_3$ (MS5) reaching a maximum of around 43 °C. This performance is considerably higher than temperature increases reported for other magnetic scaffolds, such as CS/PVA/HA composites containing 5.54 wt% SPIONs ($\Delta T \approx$ 7.5 °C)[58] and implantable poly(aspartamide)-based magneto-responsive platforms ($\Delta T \approx$ 5 °C).[59]

To provide a standardized comparison of the heating efficiency of the different magnetic nanoparticles, the Intrinsic Loss Power (ILP) values were calculated from the measured SAR values using the relation:

$$\mathrm{ILP} = \frac{\mathrm{SAR}}{H^2 \cdot f} \quad (3)$$

where H is the amplitude of the applied magnetic field and f is the field frequency. Notably, MS5 exhibited the highest ILP value (0.18 nH m^2 kg^{-1}), while MS4 showed the lowest (0.13 nH m^2 kg^{-1}), with the ILP values of all samples summarized in Table 4. These ILP values allow the performance of the nanoparticles to be evaluated independently of the specific field conditions, facilitating direct comparison with other systems reported in the literature.[58,59]

The time stability of the magnetic scaffolds was studied by determining the iron content of the supernatant after soaking the scaffold in water for three months. After this time, in MS3 sample, containing SPIONs@PEG NPs, it was visible even under naked eye that an important number of NPs was released to the solvent. On the other hand, iron in the supernatants from the

Table 5 Magnetic properties (M_s, M_r, H_c), magnetic content determined by ICP-OES, SAR, and ΔT for PU/MNP scaffolds (MS). $M_s/M_r/H_c$ were extracted from VSM hysteresis curves. Magnetothermal measurements were performed for 5 min under an alternating magnetic field of 25 mT at 253 kHz from room temperature

MS	M_s (emu g^{-1})	M_r (emu g^{-1})	H_c (Oe)	% Fe_3O_4	SAR (W g^{-1})	ILP (nH m^2 kg^{-1})	ΔT (°C)
MS1	0.70	0.04	29.48	1.02	4.51	0.05	10.47
MS2	0.90	0.01	7.18	1.32	12.64	0.13	18.30
MS3	11.44	0.22	10.50	16.11	4.69	0.05	30.74
MS4	13.86	0.13	5.40	19.25	1.33	0.01	11.18
MS5	2.40	0.04	6.56	3.92	18.21	0.18	42.86

MS5 scaffold (SPIONs@Al(OH)$_3$) was not detected by ICP-OES ([Fe] n.d.), indicating that this prototype is suitable for further characterization.

Mercury porosimetry was used to complete the characterization of the PS and selected scaffold containing nanoparticles, MS5. The results confirmed the interconnectivity between pores and revealed an average porosity of 17.3% for PS and 14.7% for MS5. The values show that the presence of the nanoparticles leads to a slight decrease in the porosity.

3.4 Cytocompatibility evaluation of PU-based magnetic scaffolds

The cytocompatibility of the PU scaffold loaded with SPIONs@Al(OH)$_3$ (MS5) was assessed in comparison with the PS using the CCK-8 assay on murine NIH/3T3 fibroblasts. Both direct and indirect contact tests were conducted for 24 h to evaluate cell viability. As shown in Fig. 10, both MS5 and PS exhibited cell viability values exceeding 80% under direct contact conditions, confirming their biocompatibility.

Similarly, high viability values observed under indirect contact indicating the cytocompatibility of the systems after 24 hours of culture. This timepoint was chosen because ISO 10993-5:2009 guidelines identify it as the standard for testing whether a material can harm cells when it comes into direct or indirect contact with them.[60] Furthermore, the absence of toxic effects supports the effectiveness of the scaffold washing protocol implemented during synthesis, ensuring the removal of residual reagents or by-products. Comparable viability values between MS5 and PS confirm that the incorporation of SPIONs@Al(OH)$_3$ does not compromise the cytocompatibility of the composite material. In conclusion, our SPIONs@Al(OH)$_3$-loaded PU scaffolds exhibit cytocompatibility comparable to or exceeding that of similar MNPs-incorporated PU scaffolds reported in the literature,[61,62] highlighting their potential for biomedical applications.

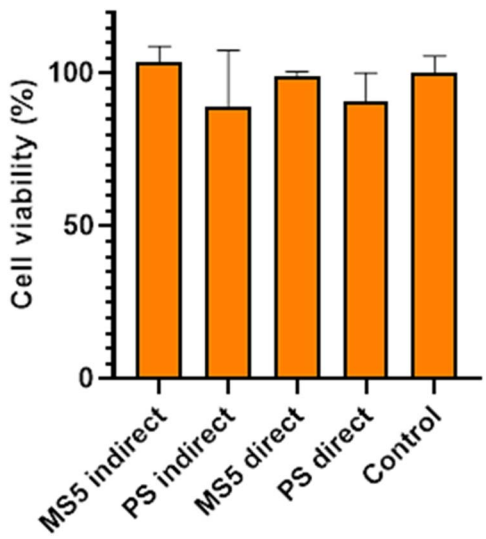

Fig. 10 Cell viability of a polyurethane scaffold (PS) and a polyurethane scaffold containing Fe_3O_4@Al(OH)$_3$ NPs (MS5) evaluated on murine NIH/3T3 fibroblasts for 24 h through direct and indirect contact.

4. Conclusions

In this work, SPIONs (Fe_3O_4 NPs) functionalized with different surface coatings (citrate, PEG, OA, and Al(OH)$_3$) were successfully synthesized and incorporated into a PU matrix to fabricate a series of magnetic scaffolds (MS1–MS5). The study demonstrated that surface chemistry plays a decisive role in governing scaffold stability, magnetic performance, and cytocompatibility. Among the systems investigated, PU scaffolds incorporating SPIONs@Al(OH)$_3$ exhibited the best performance, achieving $\Delta T \approx 43$ °C and an ILP value of 0.18 nH m^{-2} kg^{-1} under hyperthermia conditions, while maintaining negligible cytotoxicity. These findings highlight the advantages of combining polyurethane with surface-modified SPIONs and identify SPIONs@Al(OH)$_3$ as highly promising candidates for the development of multifunctional scaffolds for biomedical applications.

Author contributions

M. A. G. G.: conceptualization, investigation, writing – original draft and writing – review & editing. A. A. P.: conceptualization, investigation and writing – original draft. P. G. A.: investigation and writing – original draft. P. D. R.: investigation and writing – review & editing. L. C. A.: investigation. Y. P.: conceptualization, supervision, writing – review & editing and J. R.: conceptualization, supervision, writing – review & editing and funding acquisition. All authors reviewed the manuscript.

Conflicts of interest

The authors declare that they have no known competing financial interests or personal relationships that could have appeared to influence the work reported in this paper.

Data availability

The additional results supporting this article have been included as part of the supplementary information (SI). Supplementary information is available. See DOI: **https://doi.org/10.1039/d5na00605h**.

Acknowledgements

This work was partly supported by the Predoctoral Support Program 2020 and the Postdoctoral Fellowship Grant (ED481B Call 2023) from Xunta de Galicia, Spain. Funding for the CARTsol project (PLEC2022-009217) is partially acknowledged within the framework of the Strategic Research Plan 2021–2023, as part of the Recovery, Transformation, and Resilience Plan, 2022 call by the Ministry of Science and Innovation of Spain. P. García-Acevedo thanks to Axencia Galega de Innovación (Spain) for his Posdoctoral Grant (Axudas de apoio á etapa de formación posdoutoral – IN606B-2024.1).

References

1 A. K. Gupta and M. Gupta, *Biomaterials*, 2005, **26**, 3995–4021.
2 C. Blanco-Andujar, D. Ortega, P. Southern, Q. A. Pankhurst and N. T. K. Thanh, *Nanoscale*, 2015, **7**, 1768–1775.
3 H. Gavilán, S. K. Avugadda, T. Fernández-Cabada, N. Soni, M. Cassani, B. T. Mai, R. Chantrell and T. Pellegrino, *Chem. Soc. Rev.*, 2021, **50**, 11614–11667.
4 B. Thiesen and A. Jordan, *Int. J. Hyperth.*, 2008, **24**, 467–474.
5 T. D. Schladt, K. Schneider, H. Schild and W. Tremel, *Dalt. Trans.*, 2011, **40**, 6315–6343.
6 G. M. Manoj, M. Shalini, K. Thenmozhi, V. K. Ponnusamy and S. Hari, *Appl. Surf. Sci. Adv.*, 2024, **21**, 100608.
7 M. Bañobre-López, A. Teijeiro and J. Rivas, *Reports Pract. Oncol. Radiother.*, 2013, **18**, 397–400.
8 P. Szczepańczyk, K. Pielichowska and J. Chłopek, *J. Reinf. Plast. Compos.*, 2015, **34**, 1856–1870.
9 H. Janik and M. Marzec, *Mater. Sci. Eng. C*, 2015, **48**, 586–591.
10 M. A. González-Gómez, S. Belderbos, S. Yañez-Vilar, Y. Piñeiro, F. Cleeren, G. Bormans, C. M. Deroose, W. Gsell, U. Himmelreich and J. Rivas, *Nanomaterials*, 2019, **9**, 1–20.
11 P. He, Y. Zou and Z. Hu, *Hum. Vaccines Immunother.*, 2015, **11**, 477–488.
12 R. Augustine, A. Hasan, R. Primavera, R. J. Wilson, A. S. Thakor and B. D. Kevadiya, *Mater. Today Commun.*, 2020, **25**, 101692.
13 D. Hühn, K. Kantner, C. Geidel, S. Brandholt, I. De Cock, S. J. H. Soenen, P. Riveragil, J. M. Montenegro, K. Braeckmans, K. Müllen, G. U. Nienhaus, M. Klapper and W. J. Parak, *ACS Nano*, 2013, **7**, 3253–3263.
14 S. Belderbos, M. A. González-gómez, F. Cleeren, J. Wouters, Y. Piñeiro, C. M. Deroose, A. Coosemans, W. Gsell, G. Bormans and J. Rivas, *EJNMMI Res.*, 2020, **10**, 73.
15 M. Bil, J. Ryszkowska, J. A. Roether, O. Bretcanu and A. R. Boccaccini, *Biomed. Mater.*, 2007, **2**, 93–101.
16 H. Sadeghzadeh, H. D. Moghadam, A. Rahmani, D. Bakhshayesh, D. Mohammadnejad and A. Mehdipour, *Stem Cell Res. Ther.*, 2023, **14**, 1–17.
17 J. Gonçalves and P. Ferreira, *Mater. Proc.*, 2022, **8**, 26.
18 R. A. Perez, D. Patel and H. Kim, *RSC Adv.*, 2015, **5**, 13411–13419.
19 C. Shuai, W. Yang, C. He, S. Peng and C. Gao, *Mater. Des.*, 2020, **185**, 108275.
20 F. Yang, R. Zhao, J. Jia, H. Luo, P. Feng and C. Shuai, *Int. J. Biol. Macromol.*, 2025, **322**, 147009.
21 R. Massart, *IEEE Trans. Magn.*, 1981, **17**, 1247–1248.
22 C. Teijeiro-Valiño, M. A. González Gómez, S. Yáñez, P. García Acevedo, A. Arnosa Prieto, S. Belderbos, W. Gsell, U. Himmelreich, Y. Piñeiro and J. Rivas, *Nano Express*, 2021, **2**, 020011.
23 H. S. Roh, G. Kyu Choi, J. S. An, C. Moo Cho, D. Hoe Kim, I. Jae Park, T. Hoon Noh, D. W. Kim and K. Sun Hong, *Dalt. Trans.*, 2011, **40**, 6901–6905.
24 Z. Zhou, Y. Wang, Y. Qian, X. Pan, J. Zhu, Z. Zhang, Z. Qian, Z. Sun and B. Pi, *J. Biomater. Sci. Polym. Ed.*, 2020, **31**, 407–422.
25 P. Scherrer, *Math. Klasse*, 1918, **2**, 98–100.
26 E. Cheraghipour, A. M. Tamaddon, S. Javadpour and I. J. Bruce, *J. Magn. Magn. Mater.*, 2013, **328**, 91–95.
27 C. W. Lai, F. W. Low, M. F. Tai and S. B. Abdul Hamid, *Adv. Polym. Technol.*, 2018, **37**, 1712–1721.
28 A. Rajan, M. Sharma and N. K. Sahu, *Sci. Rep.*, 2020, **10**, 1–15.
29 V. S. Coker, A. M. T. Bell, C. I. Pearce, R. A. D. Patrick, G. van der Laan and J. R. Lloyd, *Am. Mineral.*, 2008, **93**, 540–547.
30 P. García Acevedo, M. A. González Gómez, Á. Arnosa Prieto, L. De Castro Alves, R. Seco Gudiña, Y. Piñeiro and J. Rivas, *Magnetochemistry*, 2022, **8**, 83.
31 J. Mürbe, A. Rechtenbach and J. Töpfer, *Mater. Chem. Phys.*, 2008, **110**, 426–433.
32 L. Wang, J. Bao, L. Wang, F. Zhang and Y. Li, *Chem.–A Eur. J.*, 2006, **12**, 6341–6347.
33 M. Srivastava, J. Singh, M. Yashpal, D. K. Gupta, R. K. Mishra, S. Tripathi and A. K. Ojha, *Carbohydr. Polym.*, 2012, **89**, 821–829.
34 S. S. Umare, R. S. Ningthoujam, S. J. Sharma, S. Shrivastava, S. Kurian and N. S. Gajbhiye, *Hyperfine Interact.*, 2008, **184**, 235–243.
35 Y. Na, S. Yang and S. Lee, *Desalination*, 2014, **347**, 34–42.
36 A. Qureashi, A. H. Pandith, A. Bashir, T. Manzoor, L. A. Malik and F. A. Sheikh, *Surf. Interfaces*, 2021, **23**, 101004.
37 Y. Junejo, A. Baykal and H. Sözeri, *Cent. Eur. J. Chem.*, 2013, **11**, 1527–1532.
38 A. Mukhopadhyay, N. Joshi, K. Chattopadhyay and G. De, *ACS Appl. Mater. Interfaces*, 2012, **4**, 142–149.
39 R. M. Patil, P. B. Shete, N. D. Thorat, S. V Otari, K. C. Barick, A. Prasad, R. S. Ningthoujam, B. M. Tiwale and S. H. Pawar, *RSC Adv.*, 2014, **4**, 4515–4522.
40 M. Mahdavi, M. Bin Ahmad, M. J. Haron, F. Namvar, B. Nadi, M. Z. Ab Rahman and J. Amin, *Molecules*, 2013, **18**, 7533–7548.
41 M. A. González-Gómez, S. Belderbos, S. Yañez-Vilar, Y. Piñeiro, F. Cleeren, G. Bormans, C. M. Deroose, W. Gsell, U. Himmelreich and J. Rivas, *Nanomaterials*, 2019, **9**, 1626.
42 P. Kucheryavy, J. He, V. T. John, P. Maharjan, L. Spinu, G. Z. Goloverda and V. L. Kolesnichenko, *Langmuir*, 2013, **29**, 710–716.
43 W. Pei, H. Kumada, T. Natusme, H. Saito and S. Ishio, *J. Magn. Magn. Mater.*, 2007, **310**, 2375–2377.
44 R. L. Rebodos and P. J. Vikesland, *Langmuir*, 2010, **26**, 16745–16753.
45 Z. Li, B. Tan, M. Allix, A. I. Cooper and M. J. Rosseinsky, *Small*, 2008, **4**, 231–239.
46 P. Bender, L. K. Bogart, O. Posth, W. Szczerba, S. E. Rogers, A. Castro, L. Nilsson, L. J. Zeng, A. Sugunan, J. Sommertune, A. Fornara, D. González-Alonso, L. Fernández Barquín and C. Johansson, *Sci. Rep.*, 2017, **7**, 1–14.
47 S. Neumann, L. Kuger, C. R. Arlt, M. Franzreb and D. Rafaja, *Sci. Rep.*, 2023, **13**, 1–14.

48 O. C. Chia, I. S. Suhaimin, S. A. Kassim, S. A. Zubir and T. K. Abdullah, *J. Phys. Sci.*, 2019, **30**, 115–126.
49 S. H. Lee, S. R. Shin and D. S. Lee, *Mater. Des.*, 2019, **172**, 107774.
50 D. A. Balaev, S. V. Semenov, A. A. Dubrovskiy, S. S. Yakushkin, V. L. Kirillov and O. N. Martyanov, *J. Magn. Magn. Mater.*, 2017, **440**, 199–202.
51 A. Tomitaka, T. Koshi, S. Hatsugai, T. Yamada and Y. Takemura, *J. Magn. Magn. Mater.*, 2011, **323**, 1398–1403.
52 M. Bloemen, W. Brullot, T. T. Luong, N. Geukens, A. Gils and T. Verbiest, *J. Nanoparticle Res.*, 2012, **14**, 1100.
53 V. C. Ferreira-Filho, B. Morais, B. J. C. Vieira, J. C. Waerenborgh, M. J. Carmezim, C. N. Tóth, S. Même, S. Lacerda, D. Jaque, C. T. Sousa, M. P. C. Campello and L. C. J. Pereira, *Molecules*, 2024, **29**, 1824.
54 C. R. Vestal and Z. J. Zhang, *J. Am. Chem. Soc.*, 2003, **125**, 9828–9833.
55 X. Cui, S. Belo, D. Krüger, Y. Yan, R. T. M. de Rosales, M. Jauregui-Osoro, H. Ye, S. Su, D. Mathe, N. Kovács, I. Horváth, M. Semjeni, K. Sunassee, K. Szigeti, M. A. Green and P. J. Blower, *Biomaterials*, 2014, **35**, 5840–5846.
56 X. Liu, Y. Zhang, Y. Wang, W. Zhu, G. Li, X. Ma, Y. Zhang, S. Chen, S. Tiwari, K. Shi, S. Zhang, H. M. Fan, Y. X. Zhao and X. J. Liang, *Theranostics*, 2020, **10**, 3793–3815.
57 R. Hergt and S. Dutz, *J. Magn. Magn. Mater.*, 2007, **311**, 187–192.
58 F. J. T. M. Tavares, P. I. P. Soares and J. C. Silva, *Int. J. Mol. Sci.*, 2023, **24**, 1128.
59 T. Veres, C. Voniatis, K. Molnár, D. Nesztor, D. Fehér, A. Ferencz, I. Gresits, G. Thuróczy, B. G. Márkus, F. Simon, N. M. Nemes, M. García-hernández, L. Reiniger, I. Horváth, D. Máthé, K. Szigeti, E. Tombácz and A. Jedlovszky-hajdu, *Nanomaterials*, 2022, **12**, 1476.
60 F. Miller, U. Hinze, B. Chichkov, W. Leibold, T. Lenarz and G. Paasche, *J. Biomed. Mater. Res. – Part B Appl. Biomater.*, 2017, **105**, 715–722.
61 M. Safi, H. Sarrouj, O. Sandre, N. Mignet and J. F. Berret, *Nanotechnology*, 2010, **21**, 145103.
62 I. Łopianiak, A. Kawecka, M. Civelek, M. Wojasiński, I. Cicha, T. Ciach and B. A. Butruk-Raszeja, *ACS Biomater. Sci. Eng.*, 2024, **10**, 4388–4399.